Supplementary Information

Highly Active and Thermally Stable Single-Atom Catalysts for High-Temperature Electrochemical Devices

Jisu Shin[1,2], Young Joo Lee[2], Asif Jan[1,3], Sung Min Choi[1], Mi Young Park[1,4], Sungjun Choi[1,5], Jun Yeon Hwang[6], Seungki Hong[6], Seung Gyu Park[6], Hye Jung Chang[7], Min Kyung Cho[7], Jitendra Pal Singh[8], Keun Hwa Chae[7], Sungeun Yang[1], Ho-Il Ji[1], Hyoungchul Kim[1], Ji-Won Son[1], Jong-Ho Lee[1], Byung-Kook Kim[1], Hae-Weon Lee[1], Jongsup Hong[9,10], Yun Jung Lee[2]*, and Kyung Joong Yoon[1,10]*

[1]Center for Energy Materials Research, Korea Institute of Science and Technology, Seoul 02792, Republic of Korea.

[2]Department of Energy Engineering, Hanyang University, Seoul 04763, Republic of Korea.

[3]Nanomaterials Science and Engineering, Korea University of Science and Technology (UST), KIST School, Seoul 02792, Republic of Korea

[4]Department of Materials Science and Engineering, Korea University, Seoul 02841, Korea

[5]Department of Chemical Engineering, Hanyang University, Seoul 04763, Republic of Korea

[6]Carbon Composite Materials Research Center, Korea Institute of Science and Technology, Jeonbuk 55324, Republic of Korea.

[7]Advanced Analysis Center, Korea Institute of Science and Technology, Seoul 02792, Republic of Korea.

[8]Pohang Accelerator Laboratory, Pohang University of Science and Technology, Pohang 37673, Republic of Korea

[9]Department of Mechanical Engineering, Yonsei University, Seoul 03722, Republic of Korea

[10]Yonsei-KIST Convergence Research Institute, Seoul 02792, Republic of Korea

*Correspondence to: kjyoon@kist.re.kr, yjlee94@hanyang.ac.kr

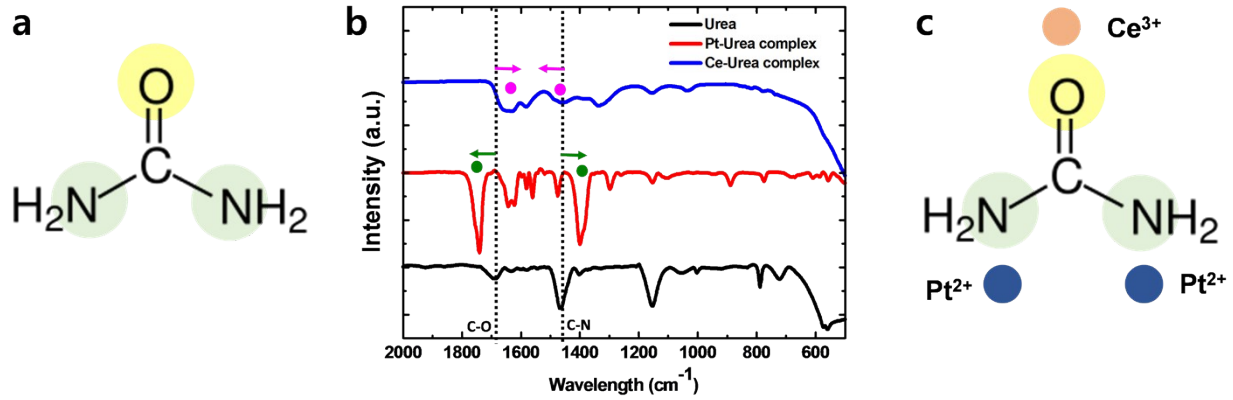

Fig. S1. Coordination of Pt and Ce to urea: (a) Molecular structure of urea showing the two types of ion-coordination sites: carbonyl O and amid N. (b) FTIR spectra of urea, Pt–urea complex, and Ce–urea complex. Coordination to the oxygen atom shifts the C–O and C–N stretching peaks to lower and higher frequencies, respectively. Coordinating to the N atom results in the opposite effect[1]. The infrared spectra confirm that Ce and Pt ions coordinate to O and N, respectively, in urea. (c) Schematic diagram showing Pt^{2+} and Ce^{3+} ion coordination to urea. During our urea-assisted method, Pt and Ce ions simultaneously coordinate with a single urea ligand, creating a strong Pt–Ce complexing effect.

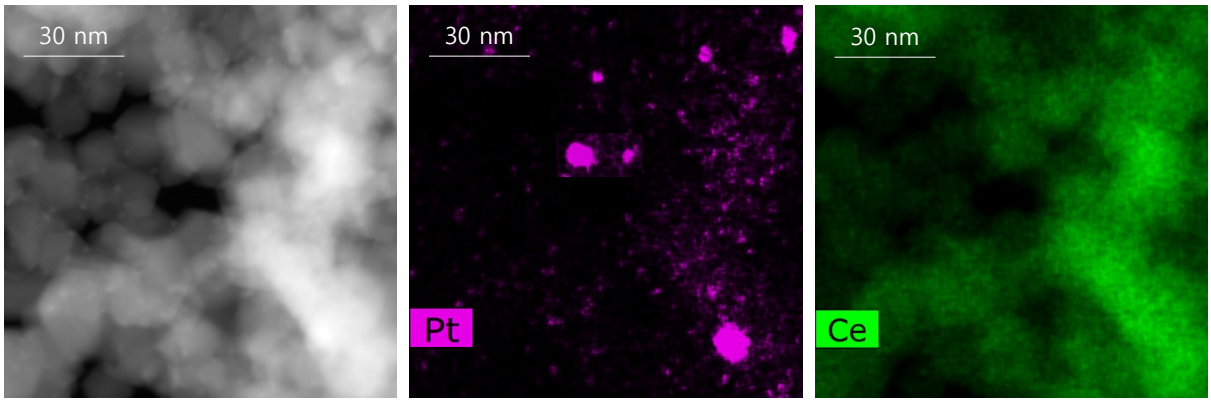

Fig. S2. TEM/EDS elemental mapping results of Pt/ceria sample synthesized without urea and calcined at 600°C in air for 1h, showing 10-20 nm sized Pt particles separated from ceria.

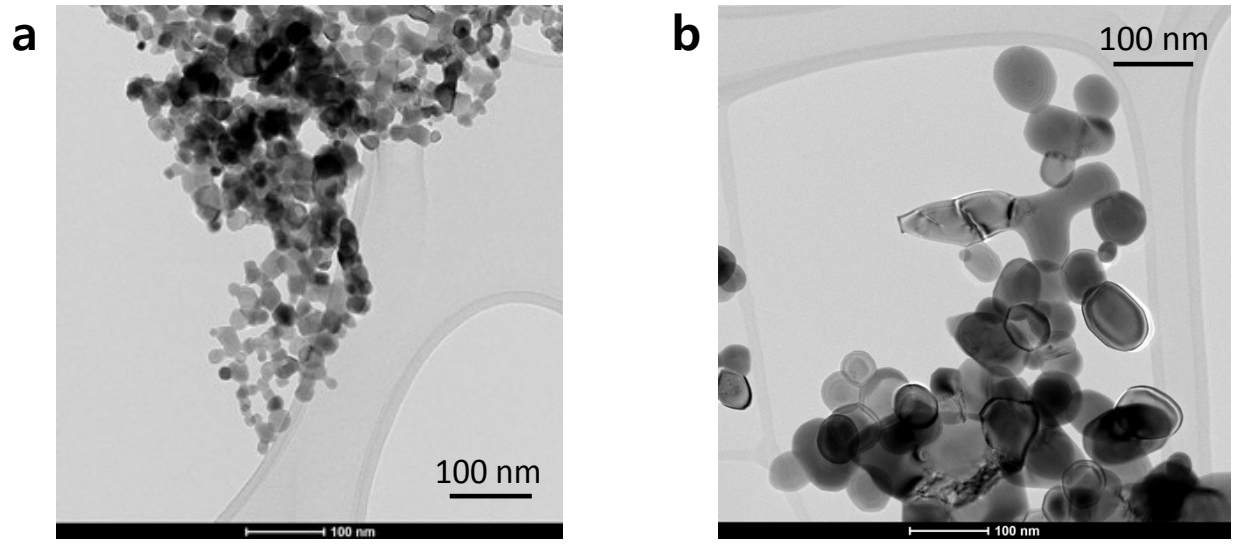

Fig. S3. Effect of urea on particle morphology: Bright-field TEM images showing the morphological characteristics of Pt/ceria nanoparticles synthesized (a) with and (b) without urea.

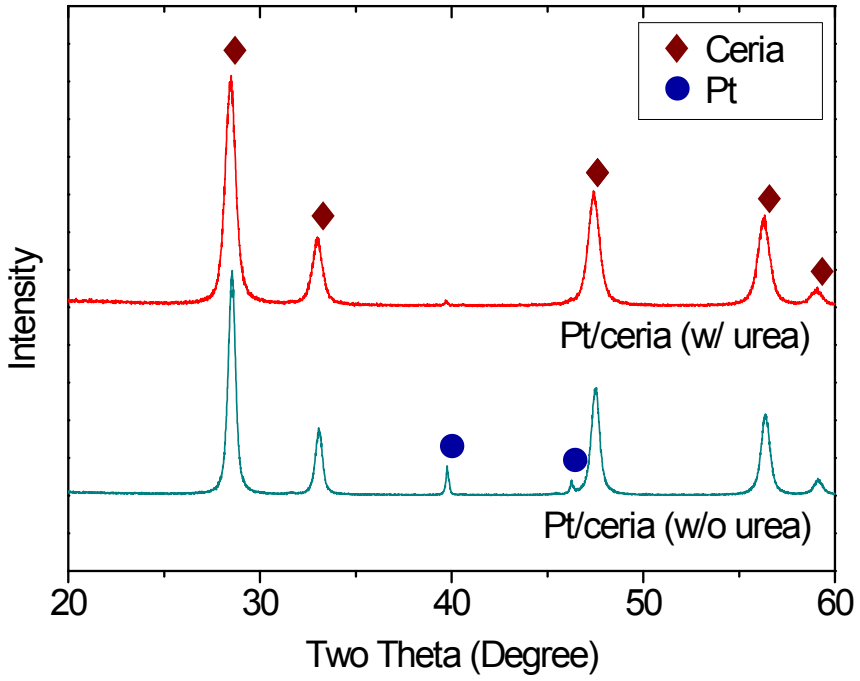

Fig. S4. Effect of urea on the formation of Pt metal phase: XRD patterns of Pt/ceria nanoparticles synthesized with and without urea.

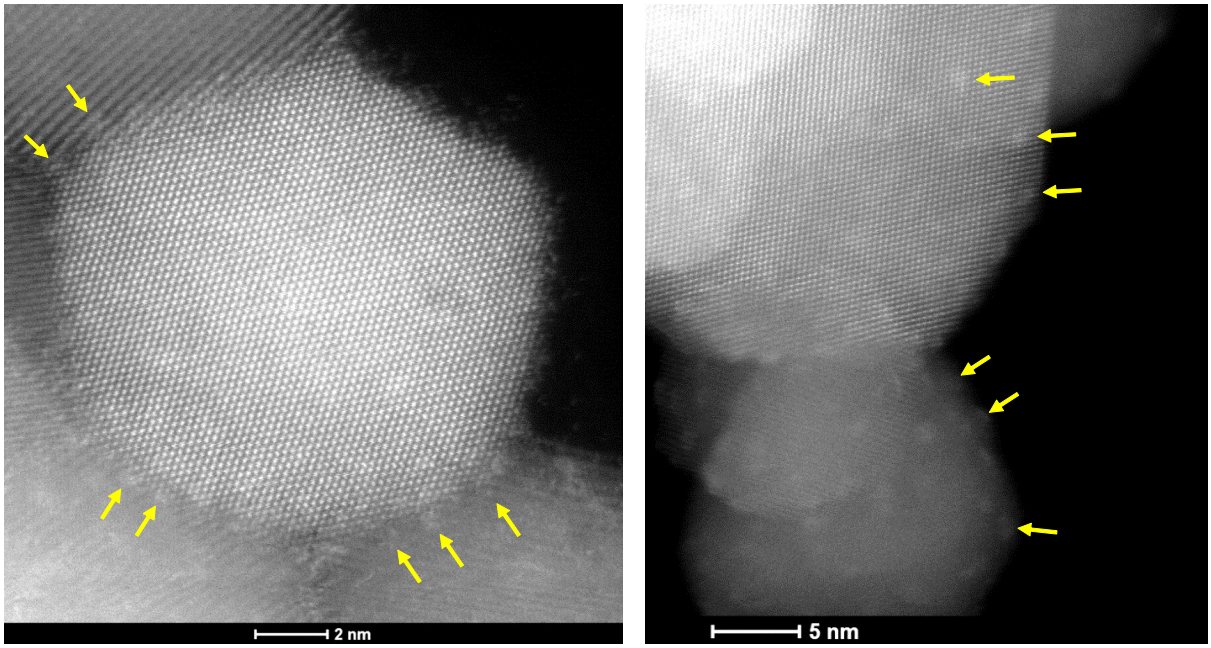

Fig. S5. Formation of Pt atomic clusters: Atomic-scale HAADF-STEM images showing atomic clusters of Pt on the ceria particle surface (partially marked with yellow arrows).

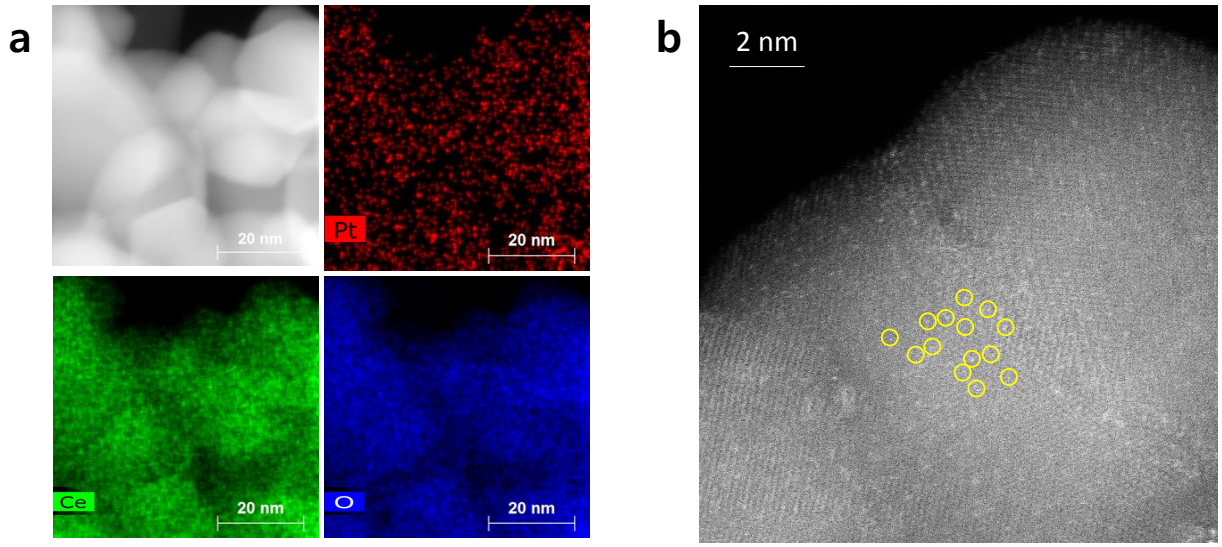

Fig. S6. Presence of isolated Pt atoms after reduction at 700°C in H_2 / 3% H_2O for 2 h: (a) TEM/EDS elemental mapping results and (b) HAADF-STEM images. Isolated Pt atoms are partially marked by yellow circles. Atomically dispersed states of Pt are maintained in reducing environments.

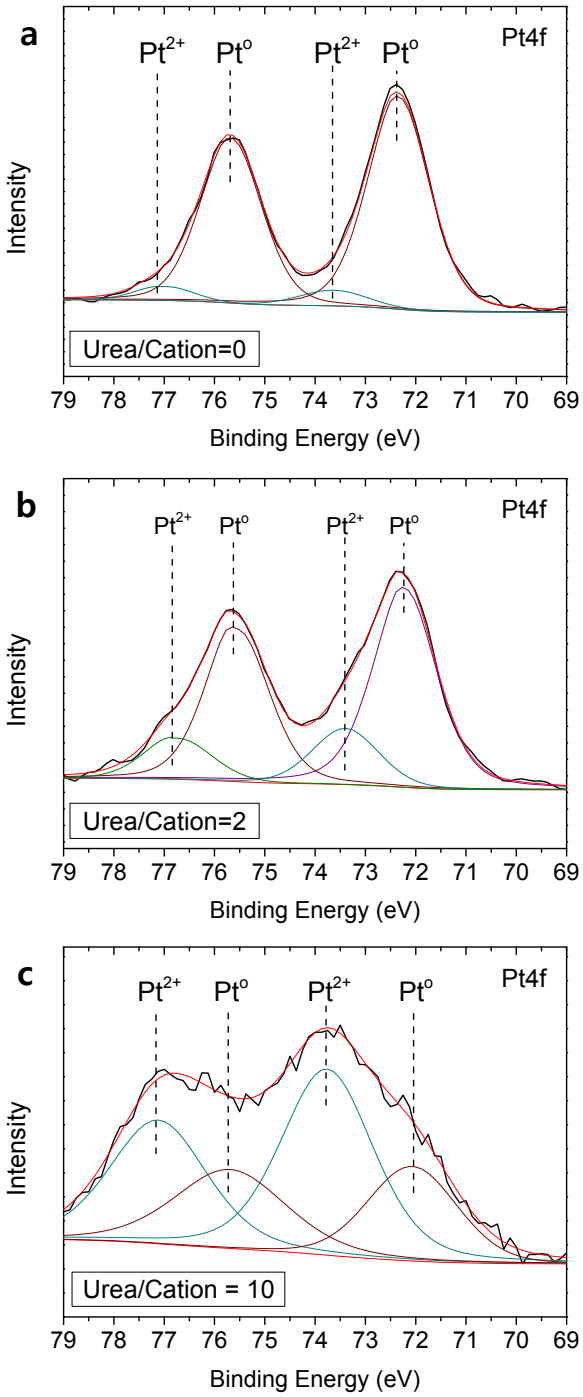

Fig. S7. Electronic structure of Pt investigated by XPS: Deconvoluted XPS spectra of Pt/ceria synthesized with urea-to-cation ratio of (a) 0, (b) 2 and (c) 10. Without urea, Pt is mostly metallic. With increasing the amount of urea, the portion of Pt^{2+} gradually increases at the expense of metallic Pt. When sufficient amount of urea is used, ionic and metallic Pt coexist, and Pt^{2+} is the major species.

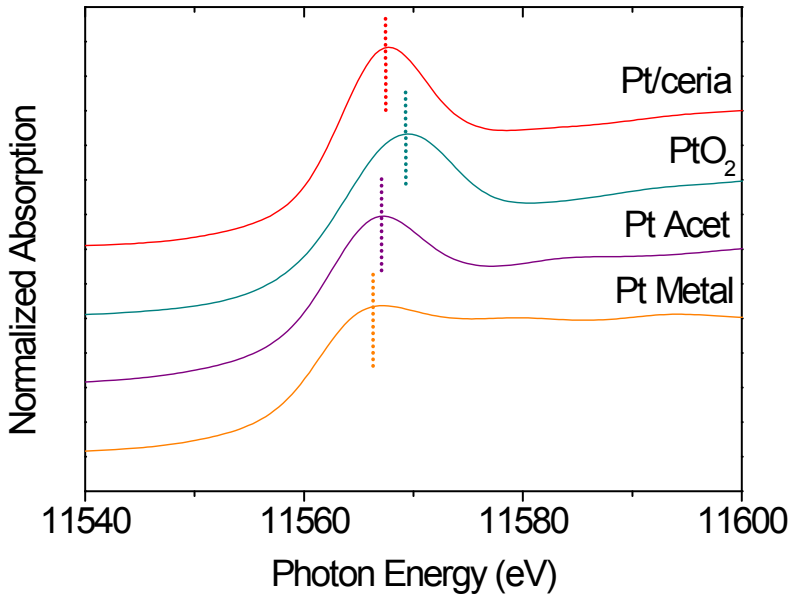

Fig. S8. Electronic structure of Pt investigated by XANES: Normalized Pt L_3-edge XANES spectra of single-atom Pt/ceria and model compounds (Pt metal, Pt acetylacetonate (Pt acet), and PtO_2). For Pt/ceria, the absorption intensity of the white line, which reflects that the electron transition from 2p to 5d orbitals of the Pt atom[2], is significantly higher than that of metallic Pt, indicating that Pt(5d) orbital is unoccupied, and a significant portion of Pt is present in a high oxidation state. The peak position of the edge energy of single-atom Pt/ceria is closer to that of Pt acet than those of Pt metal and PtO_2, supporting that the major species is Pt^{2+}.

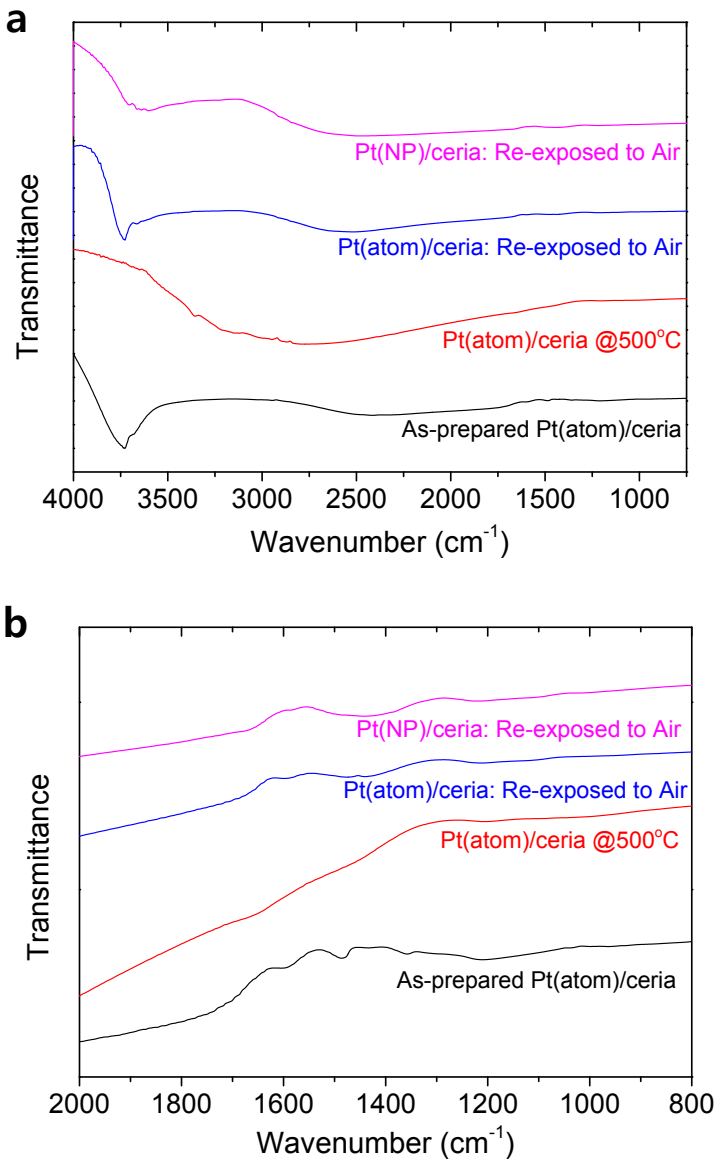

Fig. S9. FTIR spectra of single-atom Pt/ceria (Pt(atom)) collected after synthesis, at 500°C in 10% O_2-90% Ar, and after re-exposure to atmospheric air, and nanoparticle Pt supported on ceria (Pt(NP)) that was heat-treated at 500°C in 10% O_2-90% Ar and re-exposed to atmospheric air, shown in the wavenumber range of (a) 4000-750 and (b) 2000-800 cm^{-1}. The bands corresponding to carbonate species are observed at below 1800 cm^{-1} [3-5] for the as-prepared sample and removed when heated to 500°C in 10% O_2-90% Ar. Those bands are re-generated upon re-exposure to atmospheric air, and their intensities are low and similar for Pt(atom)/ceria and Pt(NP)/ceria.

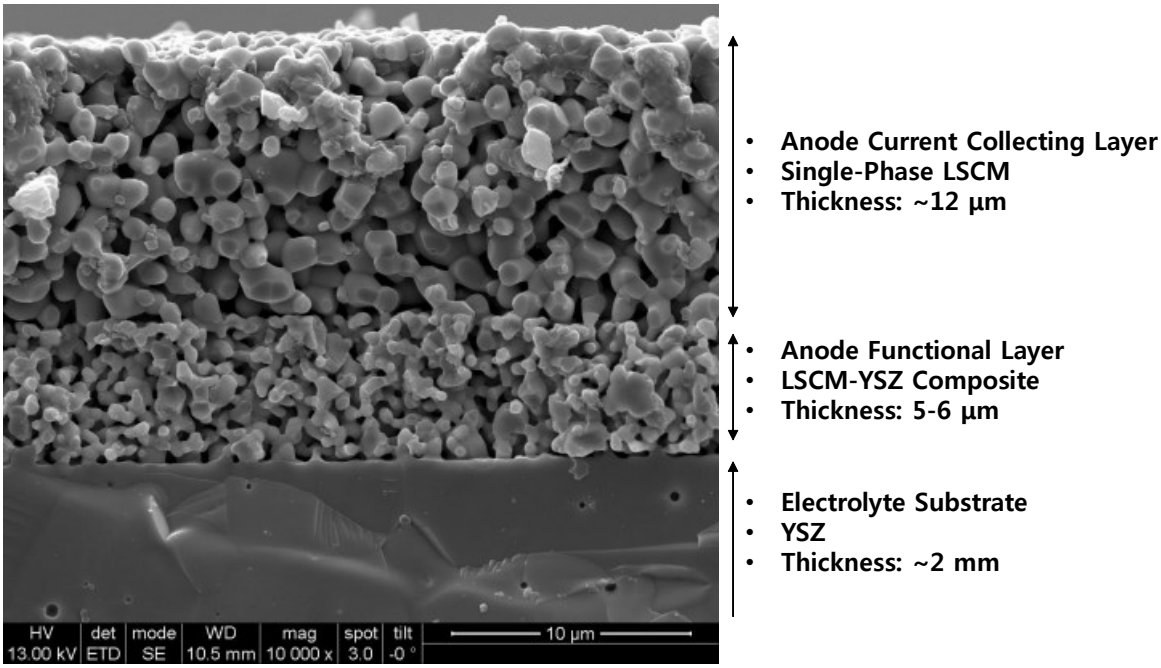

Fig. S10. Microstructure of SOC fuel electrode: SEM image of LSCM-based fuel electrode fabricated on a YSZ electrolyte substrate.

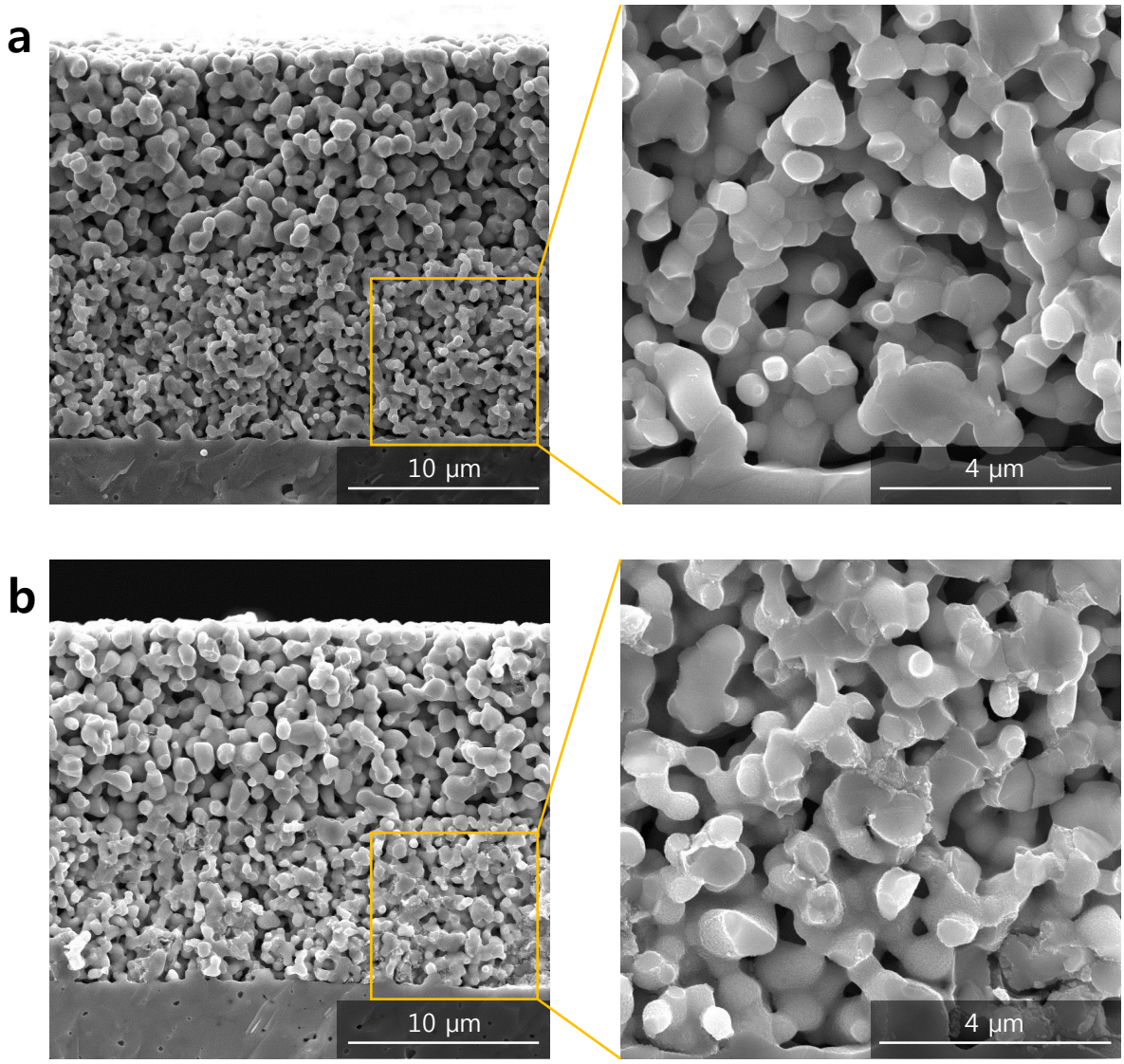

Fig. S11. SEM images of fuel electrode (a) before and (b) after infiltration. The microstructure of the fuel electrode does not change noticeably after infiltration.

a

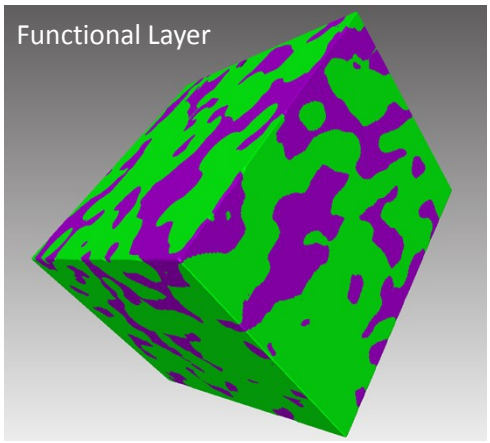

b

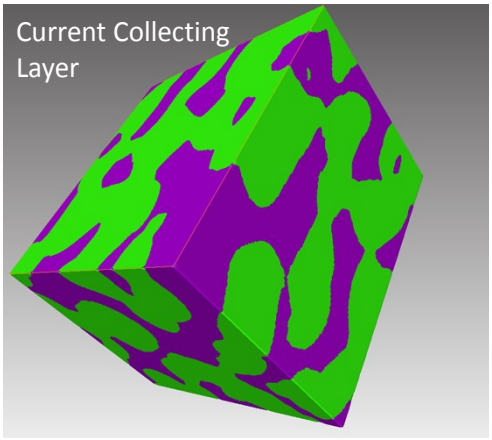

c

	Functional Layer	Current Collecting Layer
Volume Percent of Pores	34%	41%
Pore Connectivity	99.9%	99.9%
Pore Tortuosity	4.75	3.30
Surface area	2.20 $\mu m^2/\mu m^3$	1.45 $\mu m^2/\mu m^3$
Mean Ceramic Diameter	331 nm	455 nm
Mean Pore Diameter	198 nm	343 nm

Fig. S12. Microstructural analysis of functional and current collecting layers: FIB–SEM 3D reconstructed image of (a) functional and (b) current collecting layers of the LSCM fuel electrode. (c) Microstructural parameters obtained from quantitative analysis. The functional layer has a significantly finer pore structure than the current collecting layer, and this difference in the pore geometry generates capillary pressure that enables selective deposition during the infiltration process.

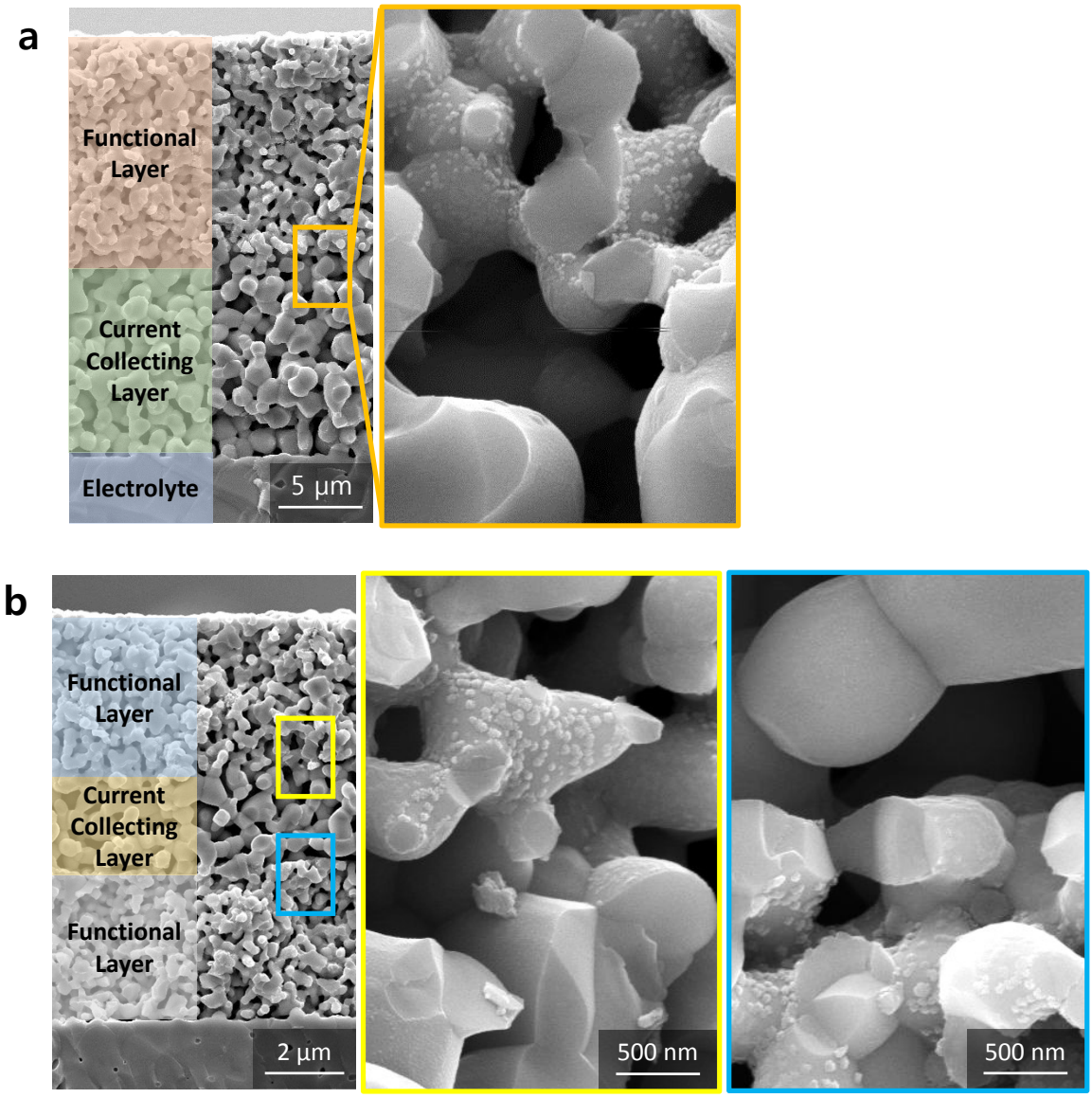

Fig. S13. SEM images showing the selective deposition of nanoparticles in various multilayer configurations: (a) Functional layer on top of the current collecting layer and (b) current collecting layer sandwiched between two functional layers. Magnified images of the interfacial regions show that nanoparticles form selectively in the functional layers.

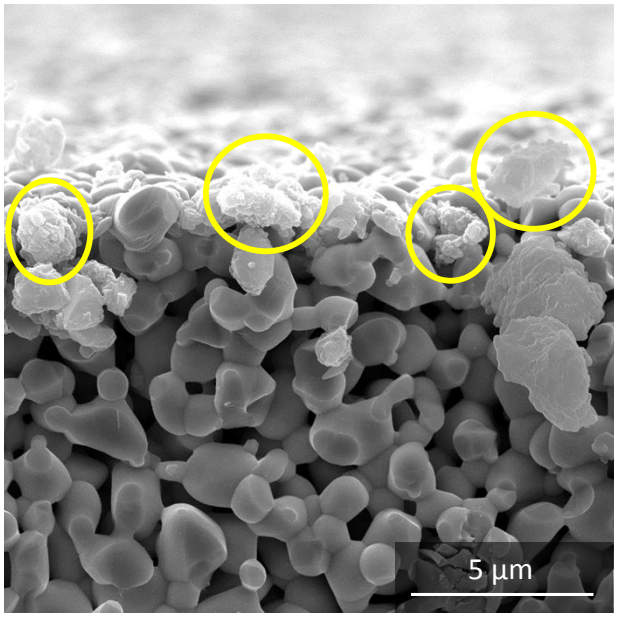

Fig. S14. SEM image showing the formation of large, aggregated particles on the outer surface of the fuel electrode current collecting layer caused by the upward convective flow during an unoptimized thermal treatment. This cell was heat-treated at 150°C after injecting the precursor solution.

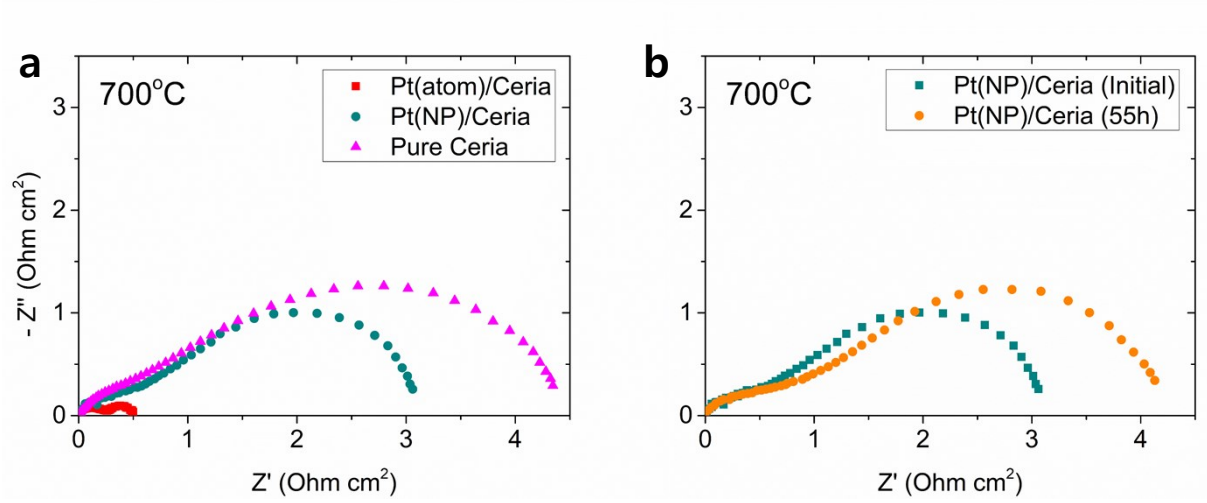

Fig. S15. (a) Impedance spectra of LSCM fuel electrodes infiltrated with pure ceria, nanoparticle Pt/ceria and single-atom Pt/ceria measured at 700°C. (b) Impedance spectra of LSCM fuel electrodes infiltrated with nanoparticle Pt/ceria measured at the initial stage and after 55h at 700°C.

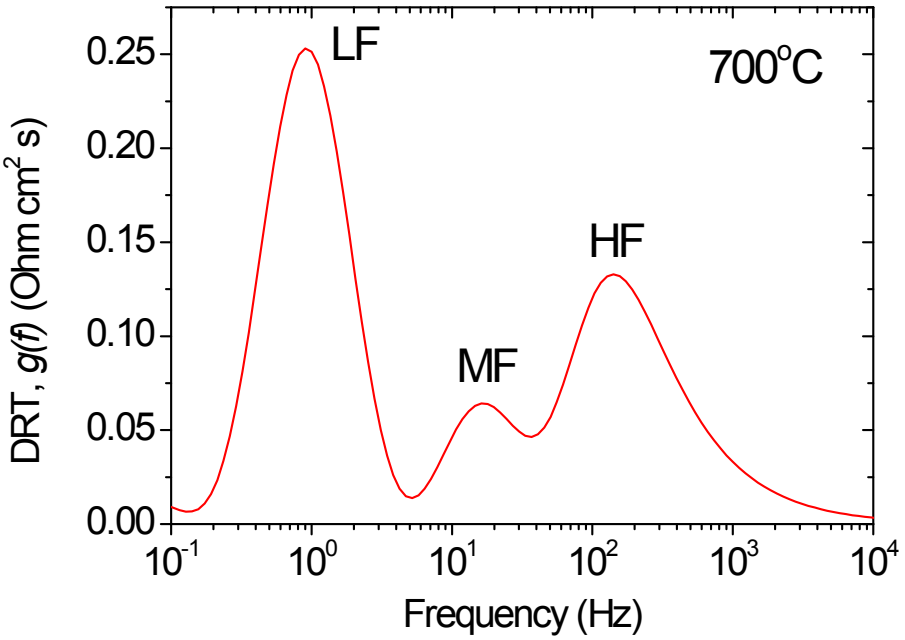

Fig. S16. Distribution function of Pt/ceria-infiltrated LSCM fuel electrode at 700°C obtained from DRT calculations. The DRT method enables directly identifying rate-limiting processes through mathematical calculations without *a priori* assumptions about the electrode processes, and multiple distinct processes within a small frequency range can be resolved owing to its high resolving capacity. The DRT calculations assume that the polarization impedance, Z_{pol}, is composed of an infinite number of *RC* elements:

$$Z_{pol} = R_{pol}\int_0^\infty \frac{\gamma(\tau)}{1+j\omega\tau}d\tau \; with \int_0^\infty \gamma(\tau)d\tau = 1 \quad (1)$$

where R_{pol} is the total polarization resistance, $\gamma(\tau)$ is the DRT, j is the imaginary unit, and ω is the angular frequency. The distribution function of a polarization process, $g(f)$, is obtained as a function of frequency, f, using the program "FTIKREG", which solves the "ill-posed inverse problem" using the Tikhonov regularization method[6]. Because the real and imaginary parts of the impedance spectra are related through the Kramers–Kronig transformations[7], only

the imaginary part was used to calculate *g(f)*. In Fig. S11, three rate-limiting processes at high, middle and low frequencies (HF, MF, and LF, respectively) are clearly identified.

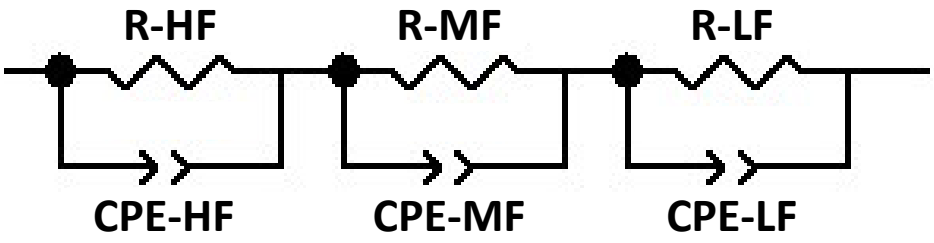

Fig. S17. Equivalent circuit model used for impedance analysis. The model is composed of three standard resistors (R)–constant phase element (CPE) units.

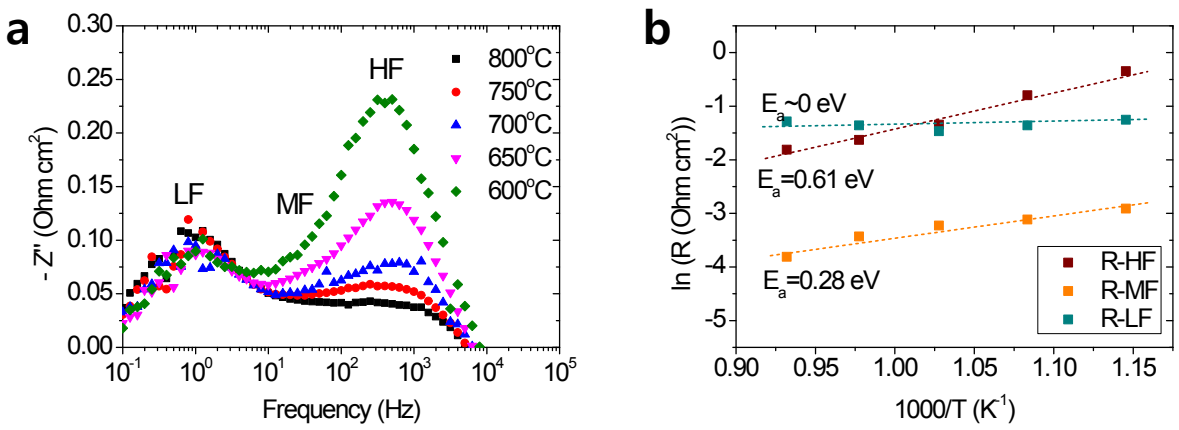

Fig. S18. Impedance analysis: (a) Bode plot of the imaginary part of the impedance and (b) Arrhenius plot of high-, mid- and low-frequency resistances of the Pt/ceria-infiltrated LSCM fuel electrode. The high- and mid-frequency impedances strongly depend on temperature, whereas the low-frequency impedance is nearly independent of temperature.

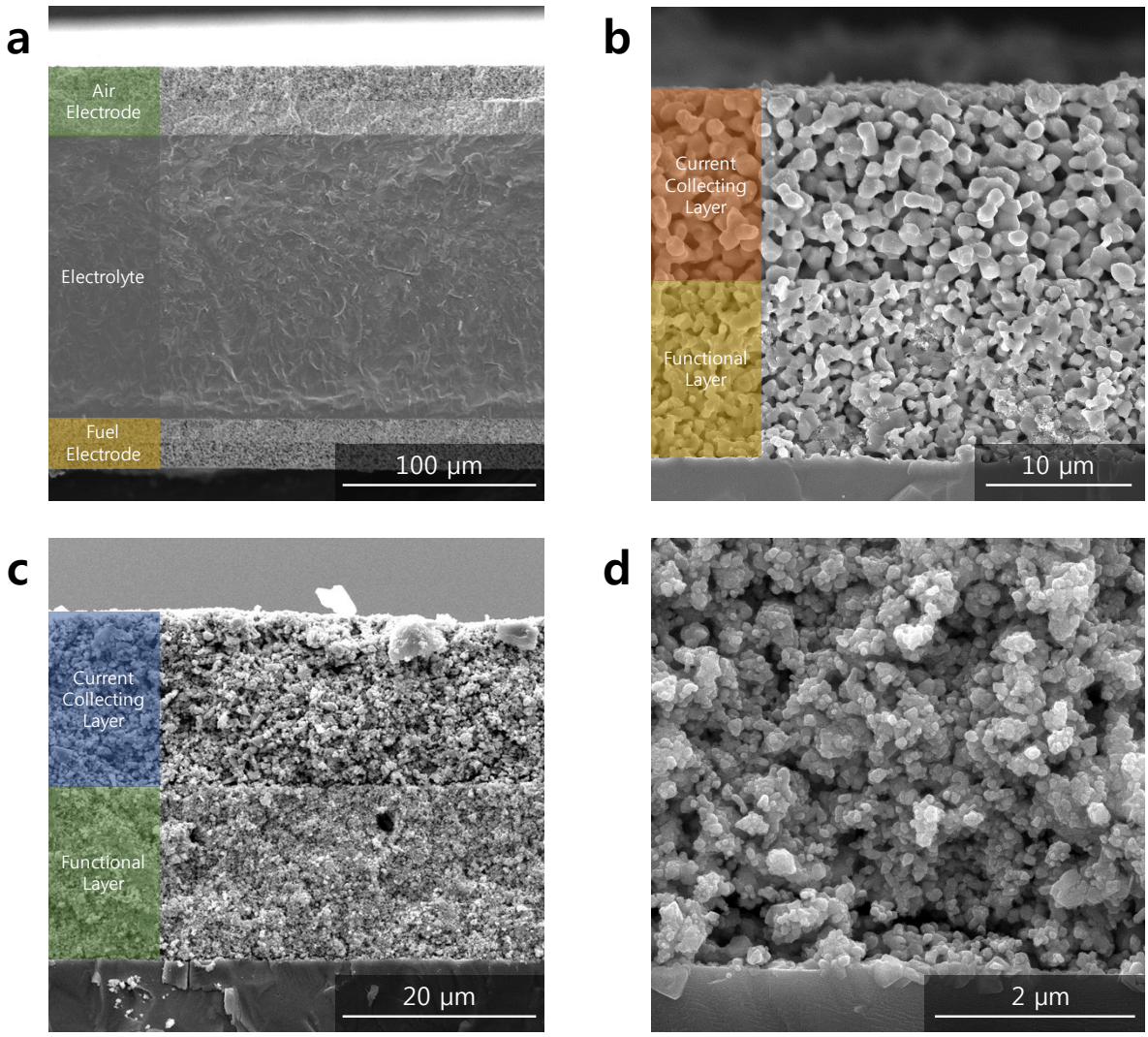

Fig. S19. SEM images of the electrolyte-supported SOC: (a) entire cell, (b) fuel electrode composed of LSCM-YSZ functional layer and LSCM current collecting layer, (c) air electrode composed of LNO-GDC functional layer and LSCF current collecting layer, and (d) SSC nanocatalysts infiltrated into air electrode.

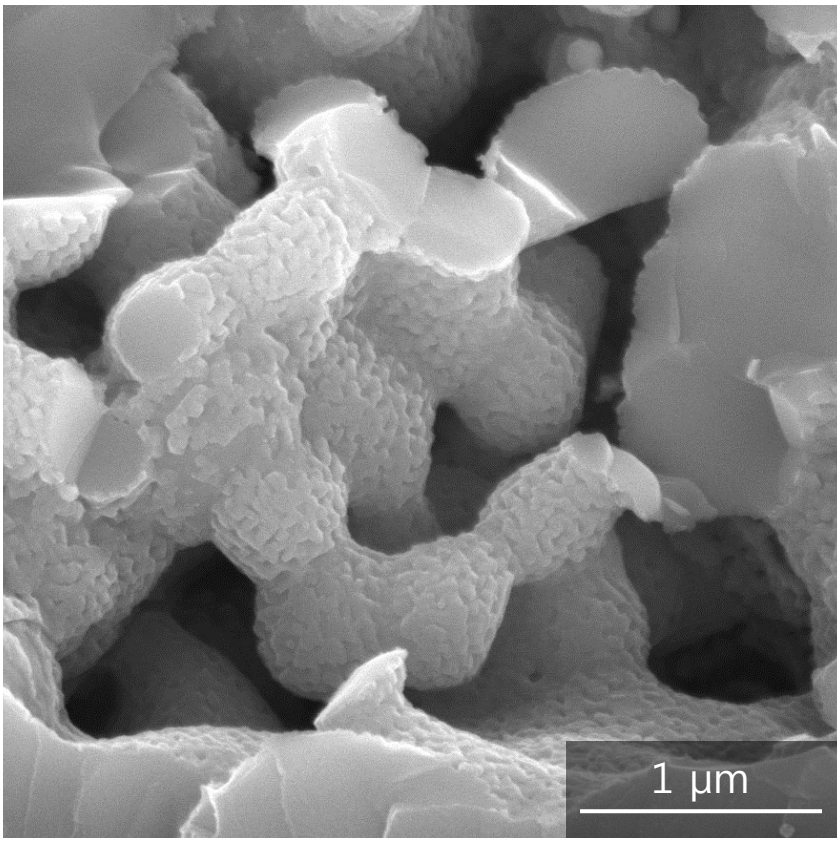

Fig. S20. SEM image of the Pt/ceria-infiltrated LSCM fuel electrode after long-term test.

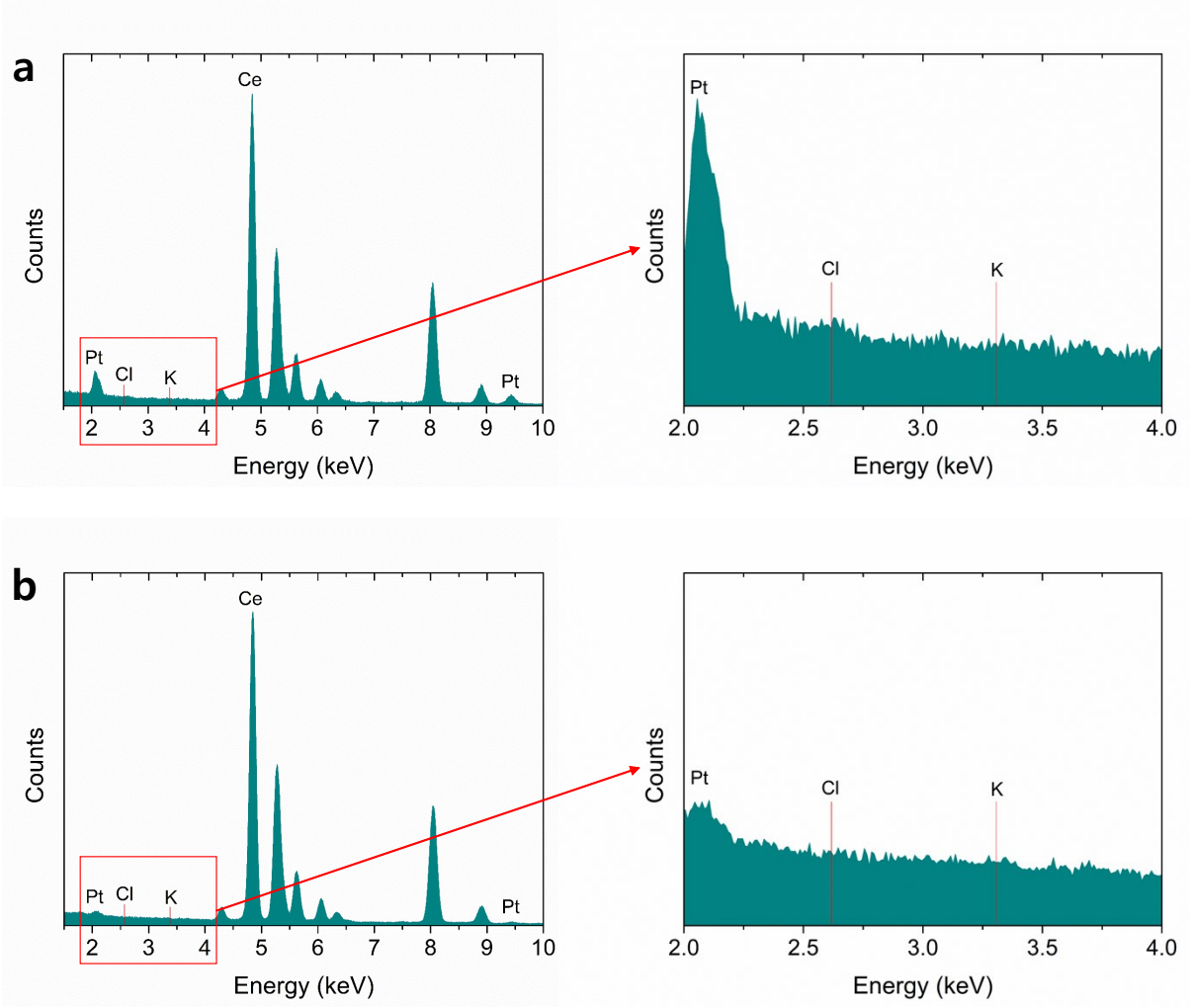

Fig. S21. EDS spectra of Pt/ceria nanoparticles synthesized (a) with and (b) without urea. No indication of residual K and Cl is found. During heat treatment at 850°C, K_2PtCl_4 thermally decomposes to form Cl_2 and KCl. Cl_2 would be removed in the gaseous form, and small amount of KCl is also expected to evaporate during heat treatment owing to its high vapor pressure at this temperature[8, 9].

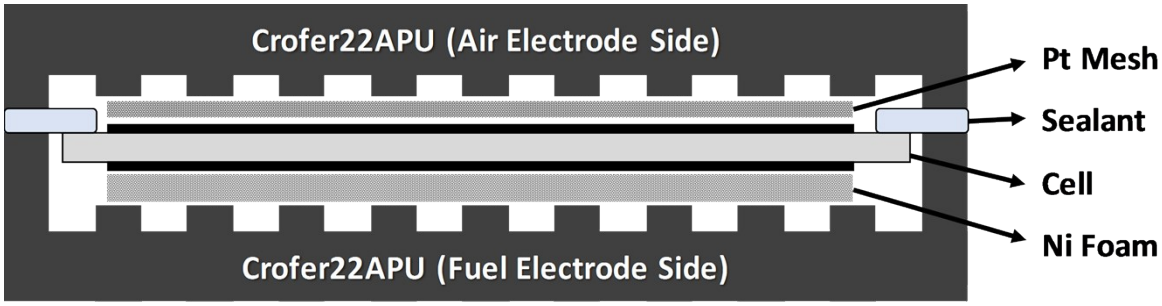

Fig. S22. Schematic of unit cell testing setup.

References

1. T. Theophanides and P. D. Harvey, *Coord. Chem. Rev.*, 1987, **76**, 237-264.
2. P. Bera, K. R. Priolkar, A. Gayen, P. R. Sarode, M. S. Hegde, S. Emura, R. Kumashiro, V. Jayaram and G. N. Subbanna, *Chem. Mater.*, 2003, **15**, 2049-2060.
3. C. Li, Y. Sakata, T. Arai, K. Domen, K.-i. Maruya and T. Onishi, *Journal of the Chemical Society, Faraday Transactions 1: Physical Chemistry in Condensed Phases*, 1989, **85**, 929-943.
4. T. Jin, Y. Zhou, G. J. Mains and J. M. White, *The Journal of Physical Chemistry*, 1987, **91**, 5931-5937.
5. T. Tanabe, Y. Nagai, T. Hirabayashi, N. Takagi, K. Dohmae, N. Takahashi, S. i. Matsumoto, H. Shinjoh, J. N. Kondo, J. C. Schouten and H. H. Brongersma, *Appl. Catal. A-Gen.*, 2009, **370**, 108-113.
6. J. Weese, *Comput. Phys. Commun.*, 1992, **69**, 99-111.
7. D. L. Misell and R. J. Sheppard, *J. Phys. D: Appl. Phys.*, 1973, **6**, 379.
8. H. Kassman, J. Pettersson, B.-M. Steenari and L.-E. Åmand, *Fuel Process. Technol.*, 2013, **105**, 170-180.
9. A. Mlonka-Mędrala, K. Gołombek, P. Buk, E. Cieślik and W. Nowak, *Energy*, 2019, **188**, 116062.